

Journal of Geophysical Research: Solid Earth

RESEARCH ARTICLE

10.1029/2017JB015394

Key Points:

- Rotary shear testing coupled with X-ray micro-CT allows for *in situ* and *in operando* observations of brittle faulting
- Real contact area consisted of contact patches that follow power law size distributions
- Large contact asperities interlock and break down during slipping, creating off-fault fractures

Supporting Information:

- Supporting Information S1
- Movie S1

Correspondence to:

Q. Zhao,
q.zhao@mail.utoronto.ca

Citation:

Zhao, Q., Tisato, N., Kovaleva, O., & Grasselli, G. (2018). Direct observation of faulting by means of rotary shear tests under X-ray micro-computed tomography. *Journal of Geophysical Research: Solid Earth*, 123, 7389–7403. <https://doi.org/10.1029/2017JB015394>

Received 27 DEC 2017

Accepted 9 AUG 2018

Accepted article online 20 AUG 2018

Published online 8 SEP 2018

Direct Observation of Faulting by Means of Rotary Shear Tests Under X-Ray Micro-Computed Tomography

Qi Zhao¹ , Nicola Tisato^{1,2} , Olga Kovaleva¹, and Giovanni Grasselli¹ 

¹Department of Civil Engineering, University of Toronto, Toronto, Ontario, Canada, ²Department of Geological Sciences, Jackson School of Geosciences, The University of Texas at Austin, Austin, TX, USA

Abstract Friction and fault evolution are critical aspects in earthquake studies as they directly influence the nucleation, propagation, and arrest of earthquake ruptures. We present the results of a recently developed experimental approach that investigates these important aspects using a combination of rotary shear testing and X-ray micro-computed tomography technology. Two sets of experiments at normal stresses (σ_n) of 2.5 and 1.8 MPa were conducted on synthetic laboratory faults. We identified real contact areas (A_c) on the fault surfaces and estimated sizes of contact patches by means of micro-computed tomography image analysis. The number of contact patches and their sizes showed positive correlations with σ_n , and contact patch size distributions followed power law relations. The total number of contact patches decreased with increasing slip distance, and large contact patches endured longer slip distance than small ones. Secondary off-fault fractures created by interlocking and breakdown of large contact patches were closely related to the sudden drops of frictional resistance, suggesting the dominant role of surface roughness on shear behavior especially at low stress.

Plain Language Summary Fault surface evolution is one of the most important but not well-understood aspects in earthquake studies. We used a novel experimental approach that combines rock physics tests with X-ray micro-computed tomography technology to improve our understanding of friction and fault surface evolution.

1. Introduction

Laboratory shear experiments have been conducted on a large variety of rocks under different conditions to study friction of faults. These studies contributed greatly to the understanding of earthquake physics (e.g., Beeler et al., 1996; Goldsby & Tullis, 2011; Mair & Marone, 1999; Marone, 1998; Reches & Lockner, 2010; Tisato et al., 2012; Toro et al., 2011). Some measurements have been the foundation of theoretical models describing friction in rocks from a microscopic perspective by considering the interaction of surface asperities (e.g., Dieterich, 1978; Sammis & Biegel, 1989). Many studies suggested that frictional behavior is intimately related to mineral composition, presence of fluids, fluid composition, and gouge material properties (e.g., Anthony & Marone, 2005; Biegel et al., 1989; Dieterich & Kilgore, 1996; Kanamori & Heaton, 2000; Mair et al., 2002; Marone & Scholz, 1989; McLaskey & Glaser, 2011; Morrow et al., 2000; Niemeijer et al., 2010a, 2010b). However, to date, these laboratory studies allowed only post-mortem examination of the deformed samples, making microscopic observation and analysis of the fault evolution challenging. Even though experiments can be performed on similar rock material at various slip distances (e.g., Hirose & Shimamoto, 2005; Tanikawa et al., 2010; Tatone & Grasselli, 2015), to characterize and observe the deformed specimen, the sample assembly is typically removed from the testing facility and opened. This may lead to the loss of fault gouge material and potential disturbance to the contacts between the opposite slipping surfaces.

X-ray micro-computed tomography (μ CT), which provides a nondestructive technique to inspect the internal structure of the sample, is increasingly used to study geomaterials (e.g., Desrues et al., 2006; Johns et al., 1993; Ketcham & Carlson, 2001; Raynaud et al., 1989; Renard et al., 2016; Ritman, 2004; Tisato et al., 2014, 2015; Vanorio et al., 2011; Viggiani et al., 2004; Zhao et al., 2015). Micro-computed tomography discretizes the sample into three-dimensional (3-D) micrometric subdomains (i.e., voxels) and measures the X-ray attenuation coefficient of each subdomain. The attenuation coefficient, usually represented by grayscale values, can be assumed to be proportional to the material density (Ritman, 2004). Zhao et al. (2017) developed a new rotary

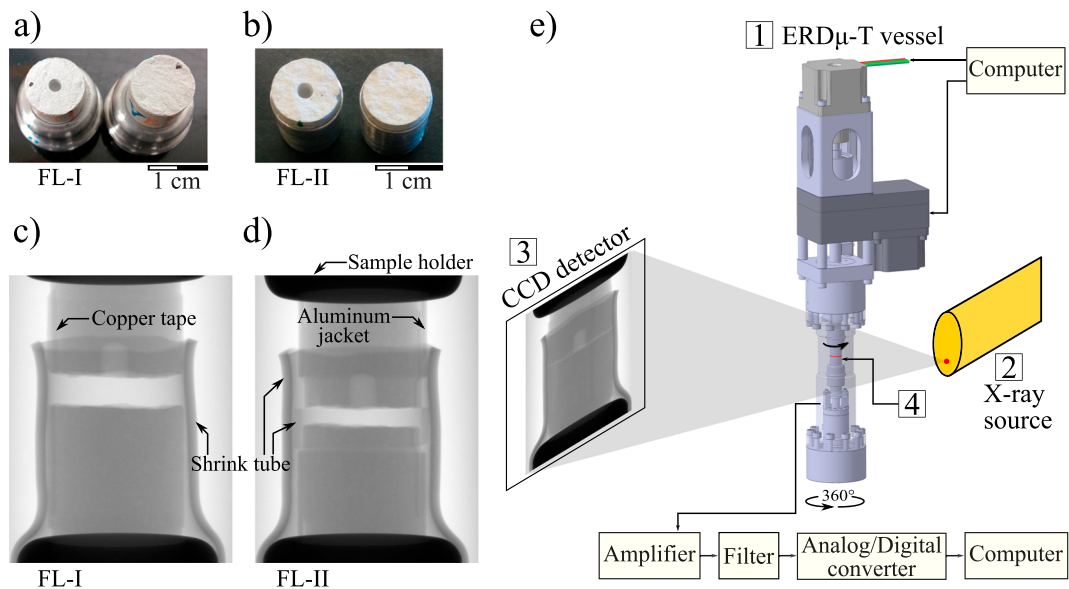


Figure 1. (a, b) Top (left) and bottom (right) semisamples of the FL-I and FL-II samples. FL-I was fixed onto the sample holders. (c, d) Two-dimensional radiographs (i.e., shadow projections) of FL-I and FL-II before testing. The gap between the top and bottom semisamples was carefully closed when applying the initial normal load. Shrink tubes were used to prevent material from escaping the gouge zone. (e) Schematic illustration of the ERDμ-T experiment setup. (1) The ERDμ-T vessel placed inside the X-ray μ CT machine, mounted on the five-axis rotation stage, (2) the X-ray source, (3) the CCD detector, and (4) the sample. CCD = charge coupled device.

shear test apparatus (ERDμ-T) that allows performing rotary shear experiments while the internal structure of the samples and the slipping surface is observed by means of μ CT.

In this study, we conducted rotary shear experiments on artificial faults (referred to as faults in the following discussion) using the ERDμ-T apparatus, and we focused on observing the evolution of slip surfaces at different slip distances without introducing disturbance to their structure. Micro-computed tomography images provided estimation of the real contact area (A_c) on the fault, and statistical analysis showed that A_c consisted of contact patches that followed power law size distributions. Moreover, data showed that interlocking between large asperities caused stress concentration that created large off-fault secondary fractures, and the formation of these new fractures caused sudden and significant friction drops.

2. Materials and Methods

2.1. Sample Preparation

The material used for the present study is a commercially available microfine calcium sulphate cement mortar named flowstone (KPM Industries, Canada). The main compositions of flowstone are bassanite ($2\text{CaSO}_4 \cdot \text{H}_2\text{O}$) and calcite (CaCO_3), and it is an appropriate replica material for the study of rock friction and shear-induced asperity degradation (Tatone, 2014; supporting information Table S1). After curing, flowstone is mechanically similar to homogeneous limestones such as the Indiana limestone (Fjar et al., 2011).

Two flowstone samples (i.e., FL-I and FL-II) were prepared and tested in this study (see supporting information for detailed sample preparation steps). Each flowstone sample was prepared to be cylindrical with 32 mm in length and 12 mm in diameter. Then the samples were transversely split into two semisamples by means of 3-point bending test (American Society for Testing and Materials, 2002). This created matching rough surfaces between the semisamples that were used as the synthetic fault (Figures 1a and 1b). Then a hole 2.5 mm in diameter and 3 mm in depth was drilled along the sample axis on the center of each top semisample. The results on FL-I suggested that at unconfined condition, fractures penetrated into the sample body and split the sample. In order to examine the influence of this secondary fracturing, FL-II was further prepared before testing by applying retaining 1 mm thick aluminum jackets 2 mm above and below the fault (Figure 1b).

Prior to the test, a strip of thin copper tape was glued vertically to the side of the recomposed sample and then cut along the fault. The copper tape served as a marker, and when the ERDμ-T vessel was closed

and placed inside the μ CT, it was visualized under the X-ray radiation allowing (1) to align the two semisamples before testing and (2) to double-check the imposed rotation of the rotating semisample with respect to the static semisample during testing. The semisamples were glued onto the sample holders with Loctite 454 Prism Instant Adhesive Gel and then mounted onto the sample holders of the ERD μ -T apparatus. In addition, a shrink tube was used to confine each sample to prevent material from escaping from the fault zone.

2.2. Shear Surface Topography Characterization

X-ray μ CT imaging has been used to quantify fracture geometry (e.g., Deng et al., 2016; Tatone & Grasselli, 2015); however, it has rarely been compared against results obtained from other high-resolution surface characterization technologies, such as, white light optical surface measurement method and laser profilometer (Brodsky et al., 2016; Tatone & Grasselli, 2009). To verify that μ CT can be used to observe and characterize surface roughness, we scanned the initial surface of the bottom semisample of FL-I using the Advanced Topometric Sensor (ATOS) II system (GOM) and compared it with the extracted surface from μ CT images.

The ATOS II system measures 3-D coordinates of the surface via the projection of various structured white-light fringe patterns onto the surface. Images of these patterns are recorded by two digital cameras from two different angles, and the 3-D coordinates of each pixel in the images are computed with high accuracy using a triangulation method and digital image processing (Tatone & Grasselli, 2009). Each ATOS II scan digitized the initial fault surface at 44- μ m horizontal grid interval with a vertical accuracy of 1 μ m. We took five scans at different angles to obtain adequate coverage of the rough surface and a dense point cloud. Then, we combined the point clouds from the five scans and interpolated them to a resolution equaled to that of the μ CT scan (i.e., 25 μ m).

On the other hand, μ CT scans at 25- μ m resolution were carried out before the top and bottom semisamples were in contact (Figures 1c and 1d), which allowed for imaging of the initial fault surfaces. The surface was segmented from the μ CT images using Otsu's thresholding method based on grayvalue histogram (Otsu, 1979).

We examined the ATOS and μ CT data sets using surface amplitude-based roughness parameters including the arithmetic mean (R_a), root mean square (R_q), maximum valley depth (R_v), maximum peak height (R_p), and the total surface amplitude (R_t ; Bhushan, 2001).

2.3. Experiment Setup and Procedure

The experiments were setup and performed following the steps described by Zhao et al. (2017; Figure 1e). For FL-I, a initial normal load of 280 N was applied, which resulted in a nominal normal stress (σ_n) of approximately 2.5 MPa. During the test, the top semisample was rotated incrementally for two 3° steps (Rot. I and II) and four 6° steps (Rot. III to VI). Experiment conducted on FL-II was carried out in a similar way but with initial $\sigma_n = 1.8$ MPa and twice the rotation step sizes. During each rotation, the top semisample was accelerated to the velocity of 3°/s in 0.1 s and stopped almost instantaneously when the desired amount of rotation was reached. The resultant averaged slip velocities for the FL-I and FL-II tests were 0.19 and 0.16 mm/s, respectively; and the resultant averaged acceleration for the FL-I and FL-II tests were 1.9 and 1.6 mm/s², respectively.

Normal force (N) and torque (M) were recorded at a sampling rate of 250 kHz, and the rotation distance was recorded every 0.06° of rotation. Note that the torque measurement signal saturated at full-scale (i.e., 1.5 N·m) during Rot. II of the FL-I test, and to avoid this from reoccurring, the voltage range of the torque acquisition channel was doubled for the successive tests.

The rotation step size was arbitrarily chosen, and after each incremental rotation step, we acquired a μ CT data set. The small rotation step size allowed for *in situ* and *in operando* imaging of the gradual morphological evolution of the sample.

3. Results and Data Analysis

3.1. Mechanical Data

The shear stress (τ) and friction (μ) were calculated using M , N , and the outer and inner radii of the shear surface (R and R_0 ; Hirose & Shimamoto, 2005; Zhao et al., 2017):

$$\tau = \frac{3M}{2\pi(R^3 - R_0^3)}, \quad (1)$$

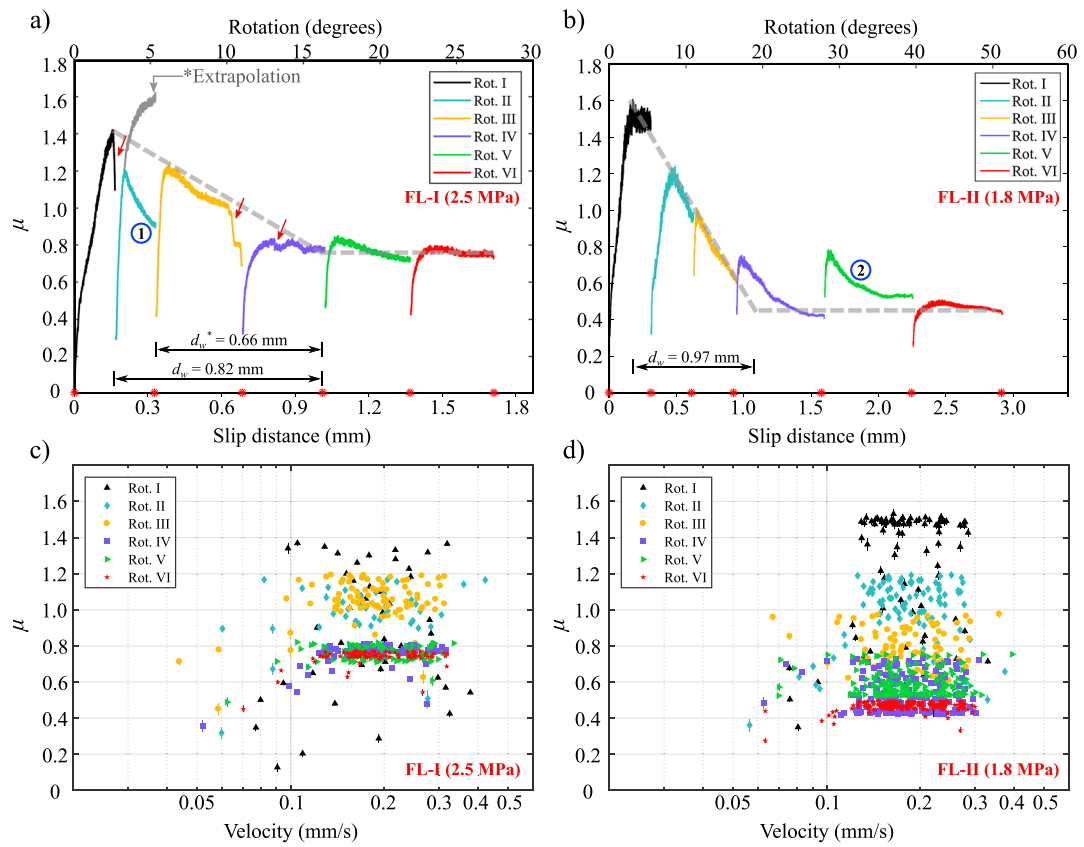


Figure 2. Friction coefficient (μ) as a function of the averaged slip distance for the experiments (a) FL-I and (b) FL-II. Red arrows indicate significant μ drops; d_w is the slip weakening parameter (equation (5)), and asterisk indicates extrapolated results. Circled numbers indicate (1) underestimated μ caused by the saturated torque measurement signal and (2) exceptionally high μ caused by the material trapped between the covering shrink tube and the sample body. The red dots on the x axes indicate where 3-D micro-computed tomography scans were carried out. The gray dashed lines show the fitted slip weakening laws. (c, d) μ versus the averaged shear velocity.

and

$$\mu = \frac{3M(R^2 - R_0^2)}{2N(R^3 - R_0^3)}. \quad (2)$$

Note that before the relative slip motion between the top and bottom fault surfaces, equation (2) provides the apparent friction coefficient that is the ratio between shear and normal stresses.

The angular rotation distance (Ω) was obtained from the voltage pulse output from the rotary motor. The averaged slip distance (d) was then calculated as

$$d = \frac{\Omega\pi(R + R_0)}{360^\circ}. \quad (3)$$

The angular rotation speed (ω) was calculated from the ratio between 0.06° (rotation monitoring interval) and the elapsed time. Then the averaged velocity (v) was calculated as

$$v = \frac{\omega\pi(R + R_0)}{360^\circ}. \quad (4)$$

In the FL-I test, for Rot. I, the initial apparent friction (μ) was 0.1. For consecutive rotation steps, the initial apparent friction coefficient varied between 0.3 and 0.5 (Figure 2a). The peak μ values recorded during the first three steps were >1 , and at the end of Rot. I, μ reached the maximum value of 1.4, after which a significant ($\sim 20\%$) drop in friction occurred. For Rot. II, the relatively low peak μ was related to the saturated torque measurement signal. Extrapolation of the torque data suggested that μ of Rot. II may reach a peak value of

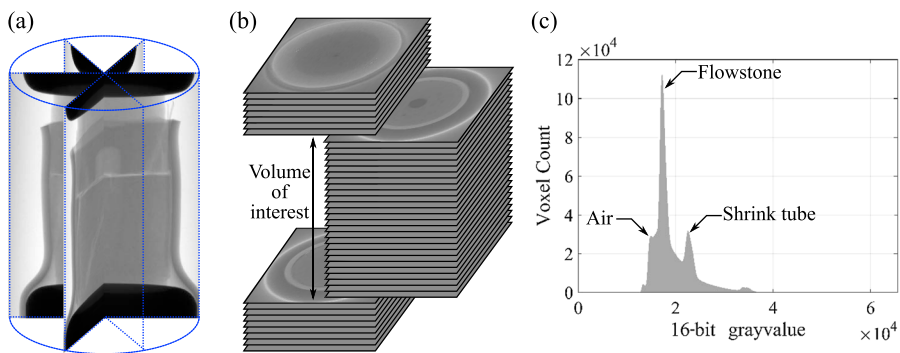


Figure 3. Micro-computed tomography image acquisition and reconstruction, taking FL-I image data as an example. (a) Two-dimensional radiographs acquired during a micro-computed tomography scan with a field of view of 794 × 1,024. (b) Reconstructed volume shown as an image stack and the 620 slices with consistent image quality were used for further analysis. (c) Histogram of the grayvalue of 620 slices showing the peaks in voxel counts that correspond to different materials.

approximately 1.6 (supporting information Figures S1 and S2). At the end of Rot. III, three consecutive μ drops occurred, and μ decreased to the residual value of approximately 0.7. During Rot. IV, a small (<10%) drop of μ occurred. During the last two rotation steps (Rot. V and VI), no significant drops were observed, and the residual μ stabilized around 0.7. In general, μ decreased gradually as a function of slip distance.

The μ measured in FL-II test showed no sudden drops (Figure 2b), and the overall trend showed a gradual decline of μ as a function of slip distance with the exception of Rot. V, which we interpreted as abnormally high because of the material trapped between the covering shrink tube and the sample body (see supporting information Figure S3). After that, the residual value of μ stabilized at approximately 0.4.

The surface roughness created shear induced dilation, which caused σ_n to increase. In the FL-I test, σ_n reached a peak value of 3.8 MPa at Rot. II, and in the FL-I test, σ_n reached a peak value of 2.6 MPa at Rot. I. Variation of σ_n may cause change of μ ; however, σ_n variation in our experiment was relatively small (<3% of the compressive strength of the material); thus, the resultant μ variation maybe small and was not considered in further discussion (Mehrishal et al., 2016).

Our experiments showed scattered μ values and high peak μ , which is common for rough surfaces at low stress conditions (Byerlee, 1978; Grasselli & Egger, 2003). We organized all the friction curves in the same time series and observed that μ had a general decay trend as a function of slip distance, resembling the slip weakening (SW) law (Andrews, 1985). Thus, we summarized the entire loading and sliding behavior in three phases (equation (5)). First, the loading phase, where apparent friction coefficient ramped up to the peak value (μ_p), this phase may be represented by a linear expression as a first approximation (Grasselli & Egger, 2003). Second, the weakening phase, where μ reduced linearly as a function of slip distance (d) from μ_p to the residual value (μ_r), with the corresponding slip distances from d_p to d_r . Third, the stable phase, where μ stabilized around μ_r .

$$\mu = \begin{cases} \frac{\mu_p}{d_p} d, & 0 < d < d_p, \\ \mu_p - (\mu_p - \mu_r) \frac{d - d_p}{d_r - d_p}, & d_p < d < d_r, \\ \mu_r, & d \geq d_r. \end{cases} \quad (5)$$

Since each rotation step had its own ramp-up phase that did not belong to a continuous shear behavior, we used the largest μ value among all steps as μ_p and the residual friction value of the successive steps to fit equation (5) (excluding FL-I Rot. II and III and FL-II Rot. V, which had abnormal frictional behaviors). Then, the distances required for μ to decrease from μ_p to μ_r were calculated as $d_w = d_r - d_p$. d_w was 0.82 mm (0.66 mm from extrapolated μ_p) and 0.97 mm for FL-I and FL-II, respectively.

It is worth mentioning that d_w should not be directly compared to the SW distance obtained in conventional experiments (e.g., Dieterich, 1978; 1979; Ruina, 1983), because we did not measure it from a continuous shear motion. Here we refer to d_w as the SW parameter, which is similar to the definition by Rabinowicz (1951). The friction coefficient was also examined against the averaged shear velocity (Figures 2c and 2d), and it showed no obvious relation with shear velocity in both experiments.

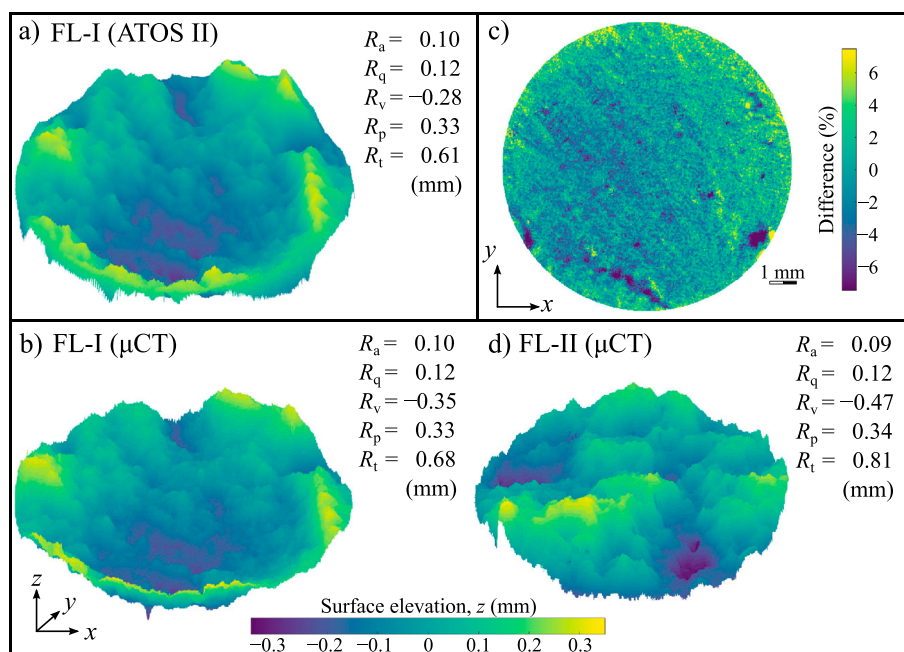


Figure 4. (a) Surface topography of FL-I obtained with the optical surface scanner (ATOS II). (b) Surface topography of FL-I extracted from μCT images. (c) Difference (i.e., mismatch) between ATOS II and μCT surface topography measurements, relative to R_t in percentage. (d) Surface topography of FL-II extracted from μCT images; (a), (b), and (d) share the same color scale. The bottom panel (b and d) demonstrates the capability of μCT in accurately imaging rough surfaces. ATOS = Advanced Topometric Sensor; μCT = micro-computed tomography.

3.2. X-Ray μCT Imaging Results

3.2.1. Reconstruction and Segmentation of μCT Images

Each μCT scan generated 1080 16-bit grayscale images having field-of-view size of $794 \times 1,024$ pixels with pixel size of $25 \mu\text{m}$ (Figure 3a). These images were reconstructed into a 3-D volume (Figure 3b) using the Phoenix X-ray datos-x-reconstruction software (v.1.5.0.22), with the following settings: a beam hardening correction of 3/10, an automatic ring artifact reduction, and a manual scan optimization that compensates for small drifts of the specimen during the scan and accurately locates the center of reconstruction (Tisato et al., 2015). The reconstructed 3-D volume composed of $1024 \times 794 \times 794$ 16-bit grayscale images, discretizing the sample into approximately 645 million voxels.

We selected the volumes of interest (i.e., adjacent to the faults and contain all fractures) from the reconstructed volumes, and then these volumes were denoised using a nonlocal means filter, segmented based on grayvalue thresholds (Figure 3c), and pore filled. A detailed image processing procedure can be found in the supporting information (Buades et al., 2005; Gonzalez & Woods, 2002).

3.3. Characterization of Shear Surface Under μCT

We first compared the optical surface scan result and μCT scan result of the bottom semisample of FL-I to verify that μCT can provide accurate surface topography measurements. The two surface measurement methods showed close results in characterizing the rough surface of FL-I (Figures 4a and 4b). In fact, the difference between the two measurements in most areas were smaller than $25 \mu\text{m}$, below the resolution of the μCT scan, and the averaged difference for the surface was $19 \mu\text{m}$ (2.8% of R_t). There were several spots of high discrepancies ($>50 \mu\text{m}$), which were related to sharp asperities and pores (Figure 4c). The same method was used to extract the initial surface of FL-II from μCT images, which showed very similar roughness to FL-I sample (Figure 4d).

3.3.1. Real Contact Area

Assessing the real contact area (A_c) is important to understand friction. Bowden and Tabor (1950) showed that the static friction coefficient is strongly dependent on A_c . A_c is often studied using transparent materials, such as polymethyl methacrylate, or inferred from indirect measurement, such as fault normal elastic stiffness (Ben-David et al., 2010; Dieterich & Kilgore, 1994; Nagata et al., 2014; Rubinstein et al., 2004; Selvadurai & Glaser, 2015). In this study, we used a novel approach to estimate A_c by means of μCT image analysis, using the following steps:

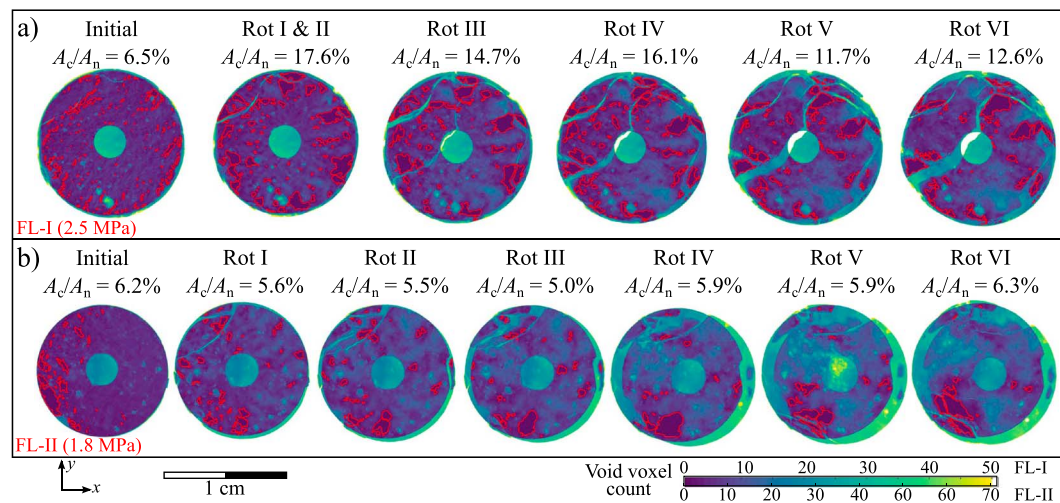


Figure 5. Real contact area at different stages of the two experiments: (a) FL-I and (b) FL-II. The color indicates the total number of voxels representing air in a specific x - y location, which can be considered as aperture height. The red contours highlight the real contact areas.

1. Horizontal segmented and pore-filled binary slices that contained the faults (50 and 70 slices for FL-I and FL-II, respectively) were inverted so that the sample material was represented by 0 and air by 1.
2. These inverted slices were then added together through a simple summation of values at the same x - y location (i.e., stacking). The stacked image was essentially a 2-D matrix representing the number of void voxels between the upper and lower walls of the fault, which can be approximated as the aperture (Figure 5).
3. In the stacked images, pixels with zeros represented the regions with no aperture or aperture size below the resolution of the μ CT scan. We consider these areas as in actual contact, and the total area associated with these pixels was considered as A_c . The ratio between A_c and the nominal contact area (A_n) was then calculated.

Only a fraction of the fault surface was in contact, and the shear and normal stresses were transmitted across the fault through contact patches (Figure 5). A_c at the initial condition was highly influenced by the sample alignment, and in both experiments, the initial contact patches were relatively small in size but significant in number comparing to other data sets. The top semisamples of FL-II was slightly tilted by $\sim 0.5^\circ$ with respect to the bottom one, which caused the fault to be preferentially loaded on one side; however, this preferred loading no longer existed after the first rotation step. Excluding the initial contact conditions, A_c/A_n ranged in 11.7–17.6% and 5.0–6.3% for FL-I (2.5 MPa) and FL-II (1.8 MPa), respectively. Namely, higher the σ_n larger the A_c .

We also investigated the real contact area by examining the characteristics of contact patches. As a first observation, some large patches may be resulted from the coalescence of contacts between closely spaced asperities. In order to avoid overestimation of the sizes and the consequent underestimation of the total number of contact patches, a marker-controlled watershed transform was applied to the image of real contact area (see supporting information for detailed procedure) before counting the total number and estimating the sizes of contact patches.

For all the slip displacements, we counted significantly more small contact patches than big ones (Figures 6a and 6b). FL-I had more than twice the total number of contact patches than FL-II, and FL-I also had more large contact patches. For both experiments, the total numbers of contact patches decreased with increasing slip distance (Figure 6c). This decrease was mostly contributed by the reduced number of small contact patches, which can be also confirmed by visual interpretation of Figure 5.

In log-log scale, the size distribution curves plateaued at the lower end and dropped rapidly at the higher end. However, the lower portion ($<0.26 \text{ mm}^2$) of each curve can be fitted by a linear relation, suggesting a self-similar (i.e., fractal) size distribution:

$$L(s) \propto s^{-m}, \quad (6)$$

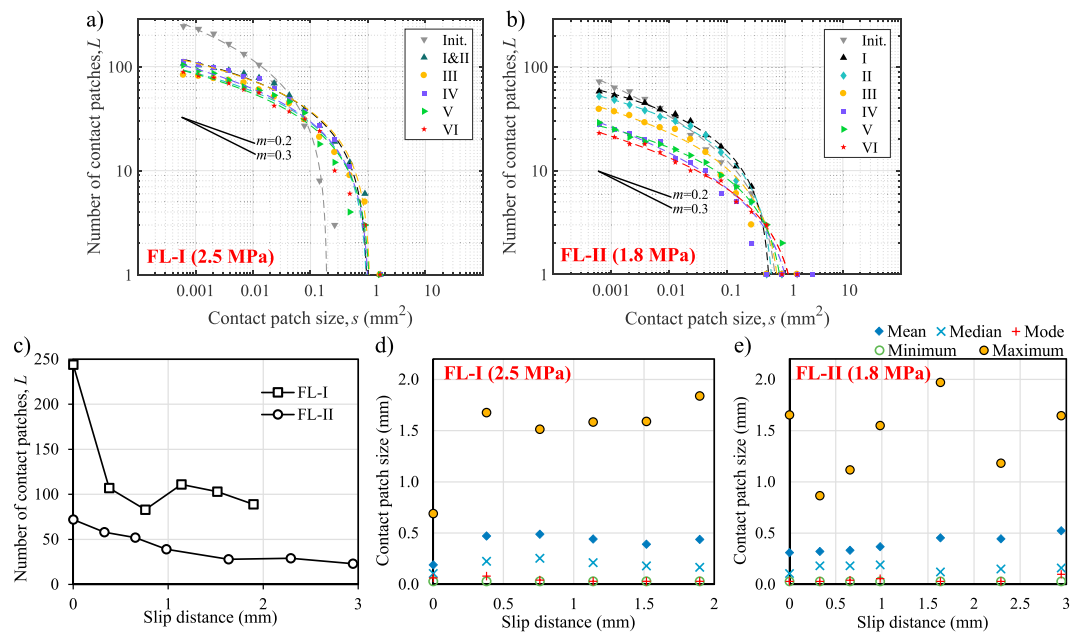


Figure 6. (a, b) Contact patch size distribution and fitted curves (dashed curves) for FL-I and FL-II tests. The lower portions of these curves can be fitted by power law relations (Table 1). (c) Number of contact patches as a function of slip distance. (d, e) Statistical parameters of the equivalent diameter of contact patches including arithmetic mean, geometric mean, harmonic mean, maximum, median, minimum, and mode. The minimum values, and in most cases the mode values, are the same, corresponding to the area of a single pixel (i.e., $25 \times 25 \mu\text{m}^2$).

where L is the cumulative number of contact patches with areas larger than contact patch size s , and m is the slope in log-log scale. Except for the initial conditions, m of FL-I and FL-II were in the ranges of 0.21 to 0.24 and 0.24 to 0.32, respectively (Table 1).

In order to further understand the size distribution of contact patches, we also tested different fitting models (see probability density functions and detailed fitting models in the supporting information Figures S8 and S9), and we found that the cumulative distribution of contact patch size is best fit by a two-term power law model:

Table 1
Summary of Fitting Parameters of the Contact Size Distribution Curves to Equations (6) and (7)

Flowstone samples	m	R_m^2	α	β	λ	R_n^2
FL-I						
Initial	0.7452	0.8870	280.7132	0.1002	-330.4927	0.9890
Rot. I&II	0.2118	0.8849	99704.5239	0.0002	-99704.4576	0.9752
Rot. III	0.2120	0.8972	26533.9980	0.0005	-26533.9712	0.9726
Rot. IV	0.2380	0.9289	43145.9379	0.0004	-43144.0289	0.9900
Rot. V	0.2103	0.9793	307.7070	0.0388	-306.9691	0.9867
Rot. VI	0.2377	0.9717	332.2179	0.0325	-330.8258	0.9907
FL-II						
Initial	0.4061	0.9691	23.4139	0.1957	-24.3347	0.9883
Rot. I	0.2631	0.9446	71604.9132	0.0001	-71609.6140	0.9959
Rot. II	0.2478	0.9443	562.4912	0.01271	-565.3939	0.9907
Rot. III	0.2975	0.8907	65.58286	0.06642	-66.0135	0.9777
Rot. IV	0.3156	0.9311	13.76693	0.15082	-12.7754	0.9802
Rot. V	0.2158	0.9598	320.4802	0.01084	-320.2476	0.9881
Rot. VI	0.2398	0.9773	23.72192	0.08895	-22.4487	0.9920

Note. R_m^2 and R_n^2 are goodness-of-fit parameters to equations (6) and (7), respectively.

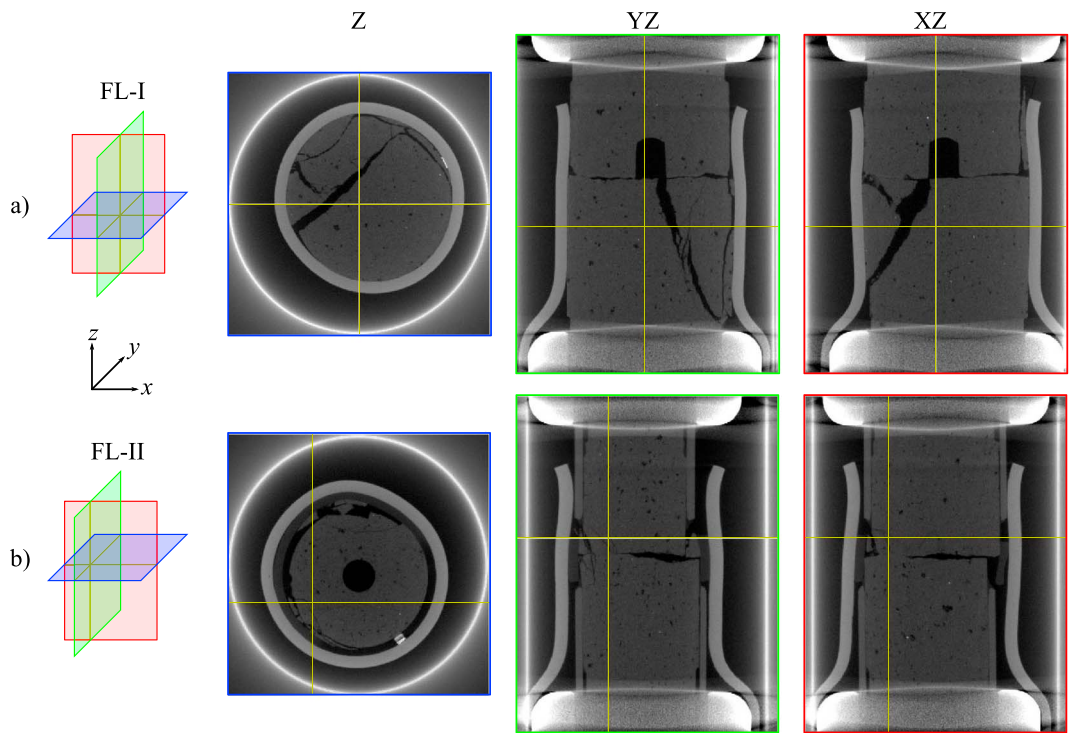


Figure 7. Selected reconstructed image slices in horizontal (Z) and vertical (YZ and XZ) directions showing the extent of the fractures at the final stage of the experiments conducted on (a) FL-I and (b) FL-II.

$$L(s) = \alpha s^{-\beta} + \lambda, \quad (7)$$

where α , β , and λ are fitted constants (Table 1).

The aspect ratio (i.e., ratio between the major axis length and the minor axis length) of contact patches of the FL-I test ranged from 1.0 to 8.4 and that of the FL-II test ranged from 1.0 to 6.7. The averaged aspect ratios of FL-I and FL-II are 6.0 and 5.6, respectively. It was suggested that SW parameter (d_w) is related to the mean dimension (i.e., diameter) of the contact junctions (e.g., Dieterich, 1979; Rabinowicz, 1951). Therefore, we further analyze the contact patches by evaluating their dimensions, and the area associated with each contact patch was converted to an equivalent diameter assuming a circular contact shape. We calculated a variety of statistical parameters of the equivalent diameters of all contact patches to obtain a good comprehension of their characteristic, which include arithmetic mean, maximum, median, minimum, and mode (Figures 6d and 6e). The equivalent diameters ranged from 0.028 to 2 mm, with mean values no more than 0.5 mm.

3.3.2. Shear-Induced Fracture and Fault Evolution

The μ CT images showed that both FL-I and FL-II experienced extensive fracturing; however, fractures in FL-I penetrated the whole sample volume and stopped close to the sample holders, while fractures in FL-II affected only a small volume near the surface due to the constrain provided by the aluminum jacket (Figure 7). In this section, we further analyzed the shear-induced fractures in the image data set of FL-I and compare it to μ variations.

To aid visual interpretation of the FL-I data set, we created the 3-D rendering of the pore-filled volume. Specifically, in order to view the fault and fractures, we represented the sample using surfaces enclosing the fractures (Figure 8). The 3-D renderings show that a fracture formed when the initial normal force was applied (Figure 8a). This fracture, considered as the initial fracture, did not fully propagate, and the segmentation procedure did not capture its whole geometry. After the first two rotation steps (Rot. I and II), the initial fracture opened and propagated causing the bottom semisample to split (Figure 8b). This fracturing process corresponded well with the μ drop at the end of Rot. I. During Rot. III, a fracture formed in the middle of the bottom semisample, and two fractures formed close to the periphery of the top semisample (Figure 8c). This series of fracturing was in agreement with the successive μ drops in Rot. III. During Rot. IV, a small fracture

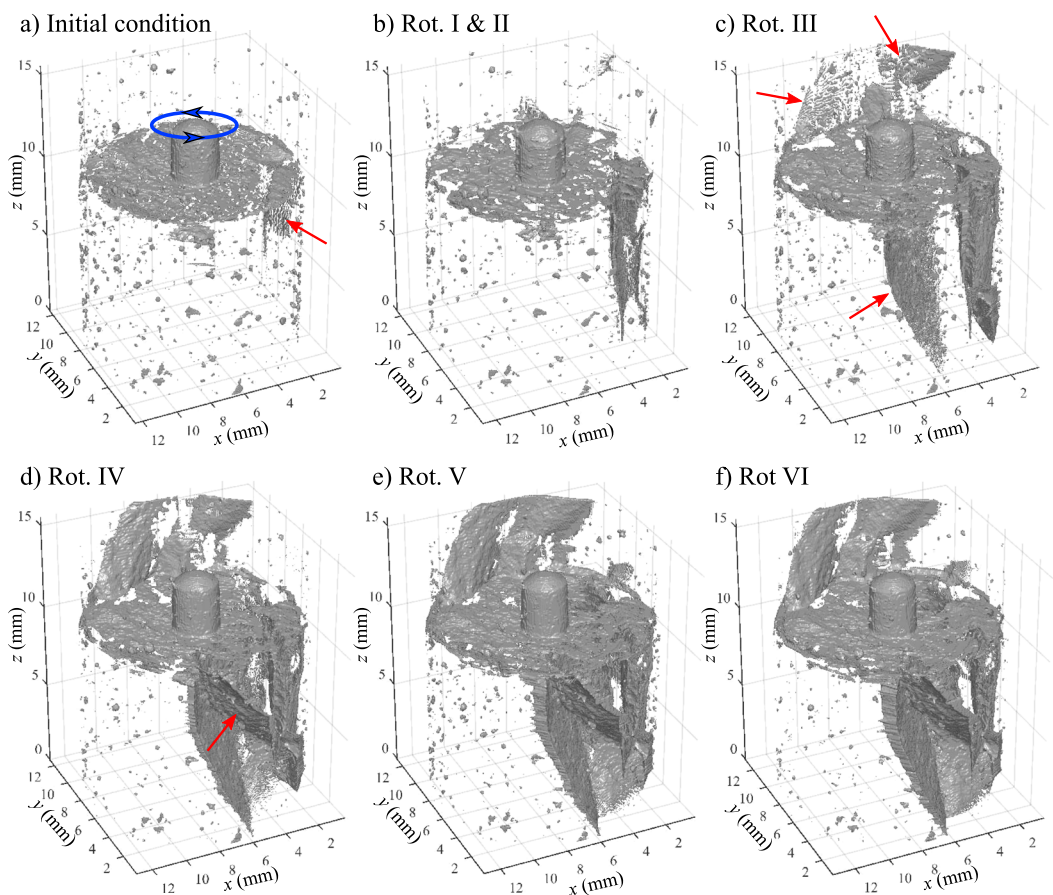


Figure 8. Three-dimensional rendering of void space surfaces in the digitized FL-I sample volume illustrating the damage process of the flowstone specimen. (a) Before the rotary shear test with 280-N normal force applied (blue arrow indicates the direction of rotation of the top semisample relative to the bottom semisample) and (b–f) after the rotation steps I–VI, respectively. Red arrows indicate the newly formed fractures in the corresponding steps. Note that the pores shown were located on the outer surface of the sample, which were not eliminated by the pore-filling process.

formed at the bottom semisample, connecting the two fractures formed in the earlier steps (Figure 8d), causing the small μ drop. During Rot. V and VI, no significant fractures were created (Figures 8e and 8f), resulting in a stable μ . However, our μ CT image data suggested that a gouge layer formed during these rotation steps.

Taking advantage of the fully digitized sample volume, we further improve our understanding of the fault evolution by extracting a circular (360°) 2-D vertical slice from the region where extensive fracturing occurred (Figure 9). To avoid loss of information due to segmentation, we used the reconstructed grayvalue image with enhanced grayvalue contrast. This 2-D slice can be viewed as a right-lateral fault, and it allowed us to observe the evolution of the shear surfaces by comparing the same 2-D slice extracted from data sets at incremental shear steps.

Although ample information can be gathered from these slices, here we list three key observations: (i) progressive aperture opening creating void space on the fault zone (i.e., blue arrows in Figure 9), (ii) the engagement of counteracting asperities and the formation of tensile secondary faulting (i.e., green arrows in Figure 9), and (iii) the degradation of the fault wall material, from intact into fine powder, forming the fault gouge (i.e., red arrows in Figure 9).

4. Discussion

4.1. Surface Roughness and Shear-Induced Damage

The comparison between the ATOS II surface scan and μ CT imaging results showed high consistency, suggesting that μ CT is a valid approach for surface roughness characterization. The discrepancies at the location of sharp asperities and pores were related to the limitations of both methods: the ATOS II system relies on the

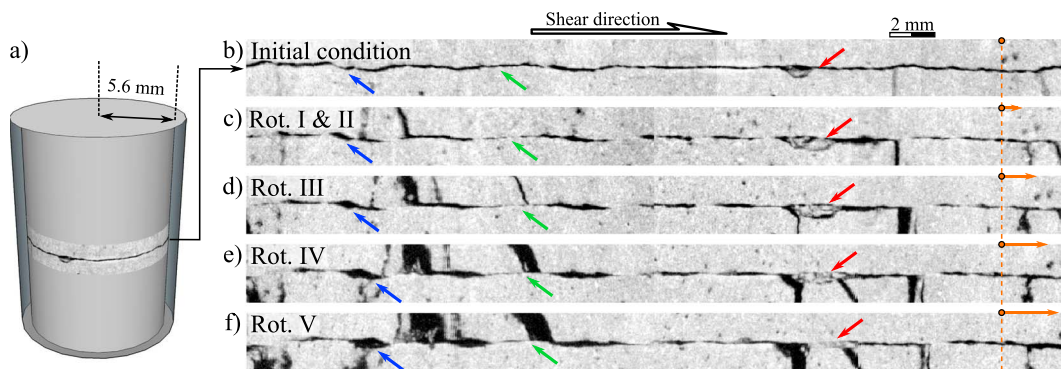


Figure 9. Expanded view of the shear surface of FL-I at the radius of 5.6 mm. (a) The extraction of the vertical 2-D slice. (b–f) The evolution of the fault viewed from the extracted slice. The hollow arrow indicates the shear direction (i.e., right lateral). Three sets of coloured arrows indicate key features: slip-induced opening (blue), induced secondary fracturing (green), and gouge formation (red). The horizontal arrows (orange) starting from the same dashed line indicate the slip distance of the top semisample relative to the bottom one.

projection of white-light fringe patterns; thus, pores that were not illuminated by the projected patterns were not captured; on the other hand, μ CT imaging smoothed sharp edges because of the spatial resolution limit. Surface roughness plays an important role in frictional behavior of rocks, especially at low stress condition (Byerlee, 1978; Grasselli & Egger, 2003). In our experiments, which were conducted at low stress (<5 MPa), significant off-fault damage (i.e., secondary fractures) was created, especially when the growth of fractures were not confined (i.e., FL-I test). The two fractures that formed in the top semisample during Rot. III and the fracture that formed in the lower semisample during Rot. IV were approximately perpendicular to the expected orientation of the least principal compressive stress (Figure 8). Interestingly, large contact patches usually appear close to these large fractures in Figure 5.

It was demonstrated that the extent of off-fault secondary fractures decreases with depth (Rice et al., 2005). Based on our observation, we suggest that the influence of secondary fracturing on frictional behavior may be more essential at shallow depth or close to surface (i.e., low confining pressure), and as the depth increase (i.e., higher confining pressure), secondary fracturing is restricted and becomes less influential to the frictional behavior. Moreover, large contact asperities interactions may be closely related to the off-fault secondary fractures, while small contact asperities may be shear off and contribute to the near-fault damage and the formation of gouge. Understanding of the spatial distribution and geometry of off-fault damage can help to characterize fault growth processes and the subsequent fault zone property variations (Mitchell & Faulkner, 2009). In an earthquake event, asperity abrasion and off-fault damage introduce additional energy sinks (Nielsen, Spagnuolo, Smith, et al., 2016; Nielsen, Spagnuolo, Violay, et al., 2016); therefore, our method may provide an approach to improve the estimation of the energy budget of the faulting process.

4.2. Friction and Fault Evolution

The ramp-up portion at the initial rotation step involves adjustment of contacts, interlocking between asperities, and dilation. The apparent friction coefficient may have reached values as high as 1.6 for both experiments, which corresponds to the similar surface roughness of the two samples. Friction coefficient (μ) scattered in a broad range, which is in agreement with the well-known data set at low stresses by Byerlee (1978).

Rapid drops of μ corresponded well with the fracturing process in the FL-I experiment, but fracturing showed no obvious impact on μ in FL-II experiment, despite the fact that both samples experienced extensive amount of fracturing and fragmentation at the shear surfaces. The reason for this difference may be twofold: First, FL-II was conducted at lower stress condition, so the sample stored less elastic strain energy before breakage; second, the aluminum jacket applied an equivalent confining pressure at the lower part of the sample that restricted the size of fractures. Therefore, the small-sized fracturing events accompanied by small energy release did not show significant influence on the friction.

We did not observe μ as low as those observed in high-velocity rotary shear experiments (e.g., Rice, 2006; Tisato et al., 2012; Toro et al., 2004, 2011; Tullis, 2007). This is because we conducted the shear test at low

velocity ($<5 \times 10^{-4}$ m/s), which is about 10^3 times slower than the critical sliding velocity for weakening mechanisms such as flash heating/melting at asperity contacts to occur (Rice, 2006). Moreover, μ showed no velocity dependency, which was in agreement with shear tests conducted on limestone at low slip rate (1.4×10^{-5} m/s; Delle Piane et al., 2016). However, note that the μ we measure may have not reached the steady state due to the small (<3 mm) slip distance.

The first several rotations all had sharp peaks of μ , and the stable friction behavior was indicated by friction curves without a sharp peak (i.e., last rotation step in both FL-I and FL-II). This is an indication of the wearing of asperities (Grasselli, 2001). Note that d_w observed from FL-I was shorter than FL-II; this may be related to the higher wearing rate at higher σ_n (Archard, 1953; Boneh et al., 2013). Moreover, the residual friction of FL-I at 0.73 was higher than that of FL-II at 0.43 (close to the internal friction of flowstone of 0.42). This suggests that FL-I may still be experiencing wearing and material degradation on the surface, even the frictional behavior was stable. This agrees with the direct observation on the fault surface (Figures 9e and 9f).

Our direct observations on the fault evolution verified some hypothesis proposed in the literature. For example, the asperity interaction mechanism proposed in the work of Boneh et al. (2014) can be observed from the 2-D slice image (Figure 9), and the creation of gouge layer from the surface wearing that lubricates the fault, as discussed in the work of Reches and Lockner (2010), was also directly observed.

4.3. Real Contact Area and Slip Weakening Parameter

Using the ERD μ -T system, we were able to imaged the incrementally sheared fault surface without perturbing its contact and stress conditions. As a result, estimation of the real contact area after each incremental slip event was achieved. At the initial condition of the experiment, the top and bottom semisamples were not in perfect matching contact due to a slight misalignment between them, which was reflected by the large numbers of small contact patches. After a small slip distance, the FL-I sample, which was tested under $\sigma_n = 2.5$ MPa, showed A_c/A_n more than double that of the FL-II sample, which was tested under $\sigma_n = 1.8$ MPa. The positive correlation between A_c and σ_n is a well-known observation (e.g., Bay & Wanheim, 1976; Logan & Teufel, 1986). Our result suggests that the increase of A_c was achieved by the increase of the total number of contact patches and their sizes. This is the first time this kind of observation has been made on nontransparent geomaterials.

Small contact patches tend to be worn out first during shearing, causing the total number of contact patches to decrease; meanwhile, larger but fewer contact patches endured longer slip distance. The observation of contact patches has important implications to the estimation of the real contact area on faults and understanding of fault slip initiation. Rabinowicz (1951) proposed the simple contact junction model that relates SW parameter (d_w) with the mean contact junction diameter. Our results suggests that this model may be improved: On one hand, the significantly large number of small contact patches account for only a small portion of the real contact area; on the other hand, large contact patches can exist for longer slip distance and play more influential role in transmitting stresses across the fault (Selvadurai & Glaser, 2016). Therefore, we suggest that large contact patches might be more influential to the slip behavior than small ones, and inferring d_w from averaged contact junction size may be an underestimation.

Natural faults have fractal grain size distribution and surface roughness (e.g., Aviles et al., 1987; Ma et al., 2006), and our results suggested that real contact area may consist of contact patches that have fractal size distribution. However, in our data, the lower end of the contact patch size distribution curve was limited by the resolution of the μ CT scan, and small contact patches were either not recognized or coalesced to be larger contact patches in the images. On the other hand, the rapid drop of the size distribution curve at the higher end was related to the limited sample size. Even though the size distribution of contact patches could be well fitted by a two-term power law, the fitted parameters did not show clear variation trends. Therefore, higher-resolution μ CT scan and larger samples may be required to capture multiscale contact conditions to further understand the distribution of contact patch sizes.

With the current ERD μ -T setup, we are limited to approximately 25- μ m resolution. Further development of our method may take advantage of nano-CT or synchrotron facilities that can reach submicron resolution. On the other hand, following Zhao et al. (2017), we were also able to capture real-time 2-D radiographies at four frames per second during the shearing process (supporting information Figure S10. Please check.). However, as the speed of fracturing and fault rupture propagation processes are at kilometers-per-second range, one might need high-energy and high-frequency synchrotron radiation techniques to capture such dynamic processes (Olbinado et al., 2017).

5. Conclusion

Friction of faults is strongly influenced by microscopic features, such as contact conditions, secondary fracturing, and gouge formation. This makes the ERD μ -T apparatus very suitable to study frictional behavior of rough rock surfaces as it allows inspecting the incremental evolution of fault surface structures, without introducing undesired perturbations. Large amounts of information can be gathered from μ CT imagery, making possible for a more comprehensive interpretation of the frictional sliding behavior than those solely relying on mechanical data.

In our experiments, the friction behavior resembled linear SW law, and abrupt drops of the friction coefficient were related to the formation of large off-fault fractures. These off-fault fractures may be caused by stress concentration due to interlocking of large asperities. We estimated the real contact areas on the fault surfaces and examined their evolution with increasing slip distances. We found that the real contact areas under 2.5- and 1.8-MPa normal stress conditions were approximately 11.7–17.6% and 5.0–6.3% of the nominal fault areas, respectively. The real contact areas consisted of contact patches that follow power law size distributions, and the exponents (i.e., slope in log-log scale) were approximately 0.2–0.3. Moreover, we found that large contact patches endured longer slip distances and may have played more important roles in controlling the slip behavior than small ones.

Acknowledgments

This work has been supported through Canada Foundation for Innovation (CFI) No. 18285, Carbon Management Canada (CMC), CMG Reservoir Simulation Foundation (FCMG), Natural Sciences and Engineering Research Council of Canada (NSERC) No. 341275, and Swiss National Scientific Foundation (SNF). Data used in this study can be accessed from our data server (<https://128.100.14.241/owncloud/index.php/s/THWqjDOJAQGMJ9D>). We thank the editors, the anonymous reviewers, and Terry Tullis at Brown University for their suggestions and constructive comments.

References

- American Society for Testing and Materials (2002). Standard test method for flexural strength of concrete (using simple beam with third-point loading) (Tech. Rep.) West Conshohocken, PA, USA: American Society for Testing and Materials.
- Andrews, D. (1985). Dynamic plane-strain shear rupture with a slip-weakening friction law calculated by a boundary integral method. *Bulletin of the Seismological Society of America*, 75(1), 1–21.
- Anthony, J. L., & Marone, C. (2005). Influence of particle characteristics on granular friction. *Journal of Geophysical Research*, 110, B08409. <https://doi.org/10.1029/2004JB003399>
- Archard, J. F. (1953). Contact and rubbing of flat surfaces. *Journal of Applied Physics*, 24(8), 981–988. <https://doi.org/10.1063/1.1721448>
- Aviles, C. A., Scholz, C. H., & Boatwright, J. (1987). Fractal analysis applied to characteristic segments of the San Andreas fault. *Journal of Geophysical Research*, 92(B1), 331–344. <https://doi.org/10.1029/JB092iB01p00331>
- Bay, N., & Wanheim, T. (1976). Real area of contact and friction stress at high pressure sliding contact. *Wear*, 38(2), 201–209. [https://doi.org/10.1016/0043-1648\(76\)90069-7](https://doi.org/10.1016/0043-1648(76)90069-7)
- Beeler, N. M., Tullis, T. E., Blanpied, M. L., & Weeks, J. D. (1996). Frictional behavior of large displacement experimental faults. *Journal of Geophysical Research*, 101(B4), 8697–8715.
- Ben-David, O., Cohen, G., & Fineberg, J. (2010). The dynamics of the onset of frictional slip. *Science*, 330(6001), 211–214.
- Bhushan, B. (2001). *Modern Tribology Handbook*. Boca Raton, FL: CRC Press.
- Biegel, R. L., Sammis, C. G., & Dieterich, J. H. (1989). The frictional properties of a simulated gouge having a fractal particle distribution. *Journal of Structural Geology*, 11(7), 827–846.
- Boneh, Y., Chang, J. C., Lockner, D. A., & Reches, Z. (2014). Evolution of wear and friction along experimental faults. *Pure and Applied Geophysics*, 171(11), 3125–3141.
- Boneh, Y., Sagy, A., & Reches, Z. (2013). Frictional strength and wear-rate of carbonate faults during high-velocity, steady-state sliding. *Earth and Planetary Science Letters*, 381(Supplement C), 127–137. <https://doi.org/10.1016/j.epsl.2013.08.050>
- Bowden, F. P., & Tabor, D. (1950). *The Friction and Lubrication of Solids*. Oxford: Clarendon Press.
- Brodsky, E. E., Kirkpatrick, J. D., & Candela, T. (2016). Constraints from fault roughness on the scale-dependent strength of rocks. *Geology*, 44(1), 19–22. <https://doi.org/10.1130/G37206.1>
- Buades, A., Coll, B., & Morel, J.-M. (2005). A non-local algorithm for image denoising. In *2005 IEEE Computer Society Conference on Computer Vision and Pattern Recognition (CVPR'05)* (Vol. 2, pp. 60–65). IEEE
- Byerlee, J. (1978). Friction of rocks. *Pure and Applied Geophysics*, 116(4-5), 615–626. <https://doi.org/10.1007/Bf00876528>
- Delle Piane, C., Giwelli, C. A., Clennell, M. B., Esteban, L., Kiewiet, L., Kager, S., & Raimon, J. (2016). Frictional and hydraulic behaviour of carbonate fault gouge during fault reactivation—An experimental study. *Tectonophysics*, 690, 21–34.
- Deng, H., Fitts, J. P., & Peters, C. A. (2016). Quantifying fracture geometry with X-ray tomography: Technique of iterative local thresholding (TILT) for 3D image segmentation. *Computational Geosciences*, 20(1), 231–244.
- Desrues, J., Viggiani, G., & Besuelle, P. (2006). *Advances in X-Ray Tomography for Geomaterials*. Wiley Online Library.
- Dieterich, J. H. (1978). Time-dependent friction and the mechanics of stick-slip. *Pure and Applied Geophysics*, 116(4-5), 790–806. <https://doi.org/10.1007/bf00876539>
- Dieterich, J. H. (1979). Modeling of rock friction: 1. Experimental results and constitutive equations. *Journal of Geophysical Research*, 84(B5), 2161–2168. <https://doi.org/10.1029/JB084iB05p02161>
- Dieterich, J. H., & Kilgore, B. D. (1994). Direct observation of frictional contacts: New insights for state-dependent properties. *Pure and Applied Geophysics*, 143(1-3), 283–302.
- Dieterich, J. H., & Kilgore, B. D. (1996). Imaging surface contacts: Power law contact distributions and contact stresses in quartz, calcite, glass and acrylic plastic. *Tectonophysics*, 256(1), 219–239.
- Fjar, E., Holt, R. M., Raaen, A. M., Risnes, R., & Horsrud, P. (2011). *Petroleum Related Rock Mechanics*. Amsterdam: Elsevier.
- Goldsby, D. L., & Tullis, T. E. (2011). Flash heating leads to low frictional strength of crustal rocks at earthquake slip rates. *Science*, 334(6053), 216–218.
- Gonzalez, R. C., & Woods, R. E. (2002). *Digital Image Processing*. Upper Saddle River, NJ: Prentice-Hall Inc.
- Grasselli, G. (2001). Shear strength of rock joints based on quantified surface description (PhD thesis), ENAC, Lausanne. <https://doi.org/10.5075/epfl-thesis-2404>
- Grasselli, G., & Egger, P. (2003). Constitutive law for the shear strength of rock joints based on three-dimensional surface parameters. *International Journal of Rock Mechanics and Mining Sciences*, 40(1), 25–40. [https://doi.org/10.1016/S1365-1609\(02\)00101-6](https://doi.org/10.1016/S1365-1609(02)00101-6)

- Hirose, T., & Shimamoto, T. (2005). Growth of molten zone as a mechanism of slip weakening of simulated faults in gabbro during frictional melting. *Journal of Geophysical Research*, 110, B05202. <https://doi.org/10.1029/2004JB003207>
- Johns, R. A., Steude, J. S., Castanier, L. M., & Roberts, P. V. (1993). Nondestructive measurements of fracture aperture in crystalline rock cores using X-ray computed tomography. *Journal of Geophysical Research*, 98(B2), 1889–1900. <https://doi.org/10.1029/92JB02298>
- Kanamori, H., & Heaton, T. H. (2000). Microscopic and macroscopic physics of earthquakes. In D. L. T. J. B. Rundle & W. Klein (Eds.), *Geocomplexity and the Physics of Earthquakes* (Vol. 120, pp. 147–163). Wiley Online Library. <https://doi.org/10.1029/GM120p0147>
- Ketcham, R. A., & Carlson, W. D. (2001). Acquisition, optimization and interpretation of X-ray computed tomographic imagery: Applications to the geosciences. *Computers and Geosciences*, 27(4), 381–400.
- Logan, J. M., & Teufel, L. W. (1986). The effect of normal stress on the real area of contact during frictional sliding in rocks. *Pure and Applied Geophysics*, 124(3), 471–485. <https://doi.org/10.1007/BF00877212>
- Ma, K. F., Tanaka, H., Song, S. R., Wang, C. Y., Hung, J. H., Tsai, Y. B., et al. (2006). Slip zone and energetics of a large earthquake from the Taiwan Chelungpu-Fault Drilling Project. *Nature*, 444(7118), 473–476.
- Mair, K., Frye, K. M., & Marone, C. (2002). Influence of grain characteristics on the friction of granular shear zones. *Journal of Geophysical Research*, 107(B10), 2219. <https://doi.org/10.1029/2001JB000516>
- Mair, K., & Marone, C. (1999). Friction of simulated fault gouge for a wide range of velocities and normal stresses. *Journal of Geophysical Research*, 104(B12), 28,899–28,914.
- Marone, C. (1998). Laboratory-derived friction laws and their application to seismic faulting. *Annual Review of Earth and Planetary Sciences*, 26, 643–696. <https://doi.org/10.1146/annurev.earth.26.1.643>
- Marone, C., & Scholz, C. H. (1989). Particle-size distribution and microstructures within simulated fault gouge. *Journal of Structural Geology*, 11(7), 799–814.
- McLaskey, G. C., & Glaser, S. D. (2011). Micromechanics of asperity rupture during laboratory stick-slip experiments. *Geophysical Research Letters*, 38, L12302. <https://doi.org/10.1029/2011GL047507>
- Mehrshal, S., Sharifzadeh, M., Shahriar, K., & Song, J. J. (2016). An experimental study on normal stress and shear rate dependency of basic friction coefficient in dry and wet limestone joints. *Rock Mechanics and Rock Engineering*, 49(12), 4607–4629.
- Mitchell, T., & Faulkner, D. (2009). The nature and origin of off-fault damage surrounding strike-slip fault zones with a wide range of displacements: A field study from the Atacama fault system, northern Chile. *Journal of Structural Geology*, 31(8), 802–816.
- Morrow, C. A., Moore, D. E., & Lockner, D. A. (2000). The effect of mineral bond strength and adsorbed water on fault gouge frictional strength. *Geophysical Research Letters*, 27(6), 815–818.
- Nagata, K., Kilgore, B., Beeler, N., & Nakatani, M. (2014). High-frequency imaging of elastic contrast and contact area with implications for naturally observed changes in fault properties. *Journal of Geophysical Research: Solid Earth*, 119, 5855–5875. <https://doi.org/10.1002/2014JB011014>
- Nielsen, S., Spagnuolo, E., Smith, S., Violay, M., Di Toro, G., & Bistacchi, A. (2016). Scaling in natural and laboratory earthquakes. *Geophysical Research Letters*, 43(4), 1504–1510. <https://doi.org/10.1002/2015GL067490>
- Nielsen, S., Spagnuolo, E., Violay, M., Smith, S., Di Toro, G., & Bistacchi, A. (2016). G: Fracture energy, friction and dissipation in earthquakes. *Journal of seismology*, 20(4), 1187–1205.
- Niemeijer, A., Marone, C., & Elsworth, D. (2010a). Fabric induced weakness of tectonic faults. *Geophysical Research Letters*, 37, L03304. <https://doi.org/10.1029/2009GL041689>
- Niemeijer, A., Marone, C., & Elsworth, D. (2010b). Frictional strength and strain weakening in simulated fault gouge: Competition between geometrical weakening and chemical strengthening. *Journal of Geophysical Research*, 115, B10207. <https://doi.org/10.1029/2009JB000838>
- Olbinado, M. P., Just, X., Gelet, J.-L., Lhuissier, P., Scheel, M., Vagoovic, P., et al. (2017). MHz frame rate hard X-ray phase-contrast imaging using synchrotron radiation. *Optics Express*, 25(12), 13,857–13,871.
- Otsu, N. (1979). A threshold selection method from gray-level histograms. *IEEE Transactions on Systems, Man, and Cybernetics*, 9(1), 62–66.
- Rabinowicz, E. (1951). The nature of the static and kinetic coefficients of friction. *Journal of applied physics*, 22(11), 1373–1379.
- Raynaud, S., Fabre, D., Mazerolle, F., Geraud, Y., & Latiere, H. J. (1989). Analysis of the internal structure of rocks and characterization of mechanical deformation by a non-destructive method: X-ray tomodensitometry. *Tectonophysics*, 159(1), 149–159.
- Reches, Z., & Lockner, D. A. (2010). Fault weakening and earthquake instability by powder lubrication. *Nature*, 467(7314), 452–455.
- Renard, F., Cordonnier, B., Dysthe, D. K., Boller, E., Tafforeau, P., & Rack, A. (2016). A deformation rig for synchrotron micromotography studies of geomaterials under conditions down to 10 km depth in the Earth. *Journal of Synchrotron Radiation*, 23(4), 1030–1034.
- Rice, J. R. (2006). Heating and weakening of faults during earthquake slip. *Journal of Geophysical Research*, 111(B5), B05311. <https://doi.org/10.1029/2005JB004006>
- Rice, J. R., Sammis, C. G., & Parsons, R. (2005). Off-fault secondary failure induced by a dynamic slip pulse. *Bulletin of the Seismological Society of America*, 95(1), 109–134.
- Ritman, E. L. (2004). Micro-computed tomography-current status and developments. *Annual Review of Biomedical Engineering*, 6, 185–208.
- Rubinstein, S. M., Cohen, G., & Fineberg, J. (2004). Detachment fronts and the onset of dynamic friction. *Nature*, 430(7003), 1005–1009. <https://doi.org/10.1038/Nature02830>
- Ruina, A. (1983). Slip instability and state variable friction laws. *Journal of Geophysical Research*, 88(B12), 10,359–10,370. <https://doi.org/10.1029/JB088iB12p10359>
- Sammis, C. G., & Biegel, R. L. (1989). Fractals, fault-gouge, and friction. In S. Mandelbrot (Ed.), *Fractals in Geophysics* (Vol. 314, pp. 255–271). Springer.
- Selvadurai, P. A., & Glaser, S. D. (2015). Novel monitoring techniques for characterizing frictional interfaces in the laboratory. *Sensors*, 15(5), 9791–9814.
- Selvadurai, P. A., & Glaser, S. D. (2016). Asperity generation and its relationship to seismicity on a planar fault: A laboratory simulation. *Geophysical Journal International*, 208(2), 1009–1025.
- Tanikawa, W., Sakaguchi, M., Tadai, O., & Hirose, T. (2010). Influence of fault slip rate on shear-induced permeability. *Journal of Geophysical Research*, 115, B07412. <https://doi.org/10.1029/2009JB007013>
- Tatone, B. S. A. (2014). Investigating the evolution of rock discontinuity asperity degradation and void space morphology under direct shear (PhD thesis), University of Toronto.
- Tatone, B. S. A., & Grasselli, G. (2009). A method to evaluate the three-dimensional roughness of fracture surfaces in brittle geomaterials. *Review of Scientific Instruments*, 80(12), 125110. <https://doi.org/10.1063/1.3266964>
- Tatone, B. S. A., & Grasselli, G. (2015). Characterization of the effect of normal load on the discontinuity morphology in direct shear specimens using X-ray micro-CT. *Acta Geotechnica*, 10(1), 31–54.

- Tisato, N., Di Toro, G., De Rossi, N., Quaresimin, M., & Candela, T. (2012). Experimental investigation of flash weakening in limestone. *Journal of Structural Geology*, 38, 183–199.
- Tisato, N., Quintal, B., Chapman, S., Madonna, C., Subramanyan, S., Frehner, M., et al. (2014). Seismic attenuation in partially saturated rocks: Recent advances and future directions. *The Leading Edge*, 33(6), 640–646.
- Tisato, N., Torriani, S. F. F., Monteux, S., Sauro, F., De Waele, J., Tavagna, M. L., et al. (2015). Microbial mediation of complex subterranean mineral structures. *Scientific Reports*, 5, 15525.
- Toro, Di., Goldsby, G. D. L., & Tullis, T. E. (2004). Friction falls towards zero in quartz rock as slip velocity approaches seismic rates. *Nature*, 427(6973), 436–439.
- Toro, Di., Han, G. R., Hirose, T., De Paola, N., Nielsen, S., Mizoguchi, K., et al. (2011). Fault lubrication during earthquakes. *Nature*, 471(7339), 494–498.
- Tullis, T. (2007). Friction of rock at earthquake slip rates. In G. Schubert (Ed.), *Treatise on Geophysics* (Vol. 4, pp. 131–152). Amsterdam: Elsevier. <https://doi.org/10.1016/B978-044452748-6.00064-X>
- Vanorio, T., Nur, A., & Ebert, Y. (2011). Rock physics analysis and time-lapse rock imaging of geochemical effects due to the injection of CO₂ into reservoir rocks. *Geophysics*, 76(5), O23–O33. <https://doi.org/10.1190/geo2010-0390.1>
- Viggiani, G., Lenoir, N., Bésuelle, P., Di Michiel, M., Marello, S., Desrues, J., et al. (2004). X-ray microtomography for studying localized deformation in fine-grained geomaterials under triaxial compression. *Comptes rendus Mécanique*, 332(10), 819–826.
- Zhao, Q., Tisato, N., & Grasselli, G. (2017). Rotary shear experiments under X-ray micro-computed tomography. *Review of Scientific Instrument*, 88(15), 110. <https://doi.org/10.1063/1.4974149>
- Zhao, B., Wang, J., Coop, M. R., Viggiani, G., & Jiang, M. (2015). An investigation of single sand particle fracture using X-ray micro-tomography. *Géotechnique*, 65(8), 625–641.